García Trenco, A.; Valencia Valencia, S.; Martinez Feliu, A. (2013). The impact of zeolite pore structure on the catalytic behavior of CuZnAl/zeolite hybrid catalysts for the direct DME synthesis. Applied Catalysis A General. 468:102-111. doi:10.1016/j.apcata.2013.08.038

The impact of zeolite pore structure on the catalytic behavior of CuZnAl/zeolite hybrid catalysts for the direct DME synthesis

Andrés García-Trenco, Susana Valencia, Agustín Martínez*

Instituto de Tecnología Química, UPV-CSIC, Avda. de los Naranjos s/n, 46022, Valencia, Spain.

*Corresponding author: amart@itq.upv.es (A. Martínez). Phone: (+34) 963877808; Fax: (+34) 963877809.

Abstract

In this work, the influence of the pore structure of 10-ring zeolites used as the methanol dehydration function in CuZnAl(CZA)/zeolite hybrid catalysts was studied for the direct dimethyl ether (DME) synthesis. To this purpose, six different 10-ring H-zeolites (ZSM-5, FER, IM-5, TNU-9, MCM-22, ITQ-2) with alike bulk Si/Al ratios (in the 9-14 range) were employed. Additionally, the effect of crystallite size (for ZSM-5) and selective surface dealumination by treatment with oxalic acid (for MCM-22) was also investigated. While the initial activity of the zeolites for methanol dehydration was driven by the concentration of strong Brønsted acid sites, the extent of decay was dictated by the pore structure, which determined the amount and nature of the formed carbon species. When evaluated for direct DME synthesis under methanol synthesis-controlled conditions, all CZA/zeolite hybrid catalysts (prepared by grinding, CZA:zeolite mass ratio of 2:1) experienced a decline of CO conversion (and DME yield) with time-on-stream (TOS) due to a gradual loss of the methanol synthesis activity of the Cu-based component. Interestingly, the stability with TOS was the lowest for the hybrid catalysts comprising zeolites with large external surface areas (S_{ext}) such as ITQ-2 and MCM-22. Moreover, for zeolites with similar S_{ext}, the deactivation extent of the hybrid catalysts increased with the concentration of surface Al species (from XPS) in the zeolite. Thus, the delaminated ITQ-2 zeolite (Si/Al_{surf}= 10.6, S_{ext}= 324 m^2/g) produced the less stable hybrid while that comprising zeolite TNU-9 (Si/Al_{surf}= 17.9, S_{ext}= 12 m^2/g) displayed the highest stability during the syngas-to-DME experiments. These results suggest that the deterioration of the methanol synthesis activity of the CZA catalyst in the hybrid catalysts prepared by grinding is produced by detrimental interactions between zeolitic Al species and Cu sites at the surface-contact between zeolite and CZA particles.

Keywords: Methanol dehydration; synthesis gas; direct DME synthesis; CuZnAl methanol synthesis catalyst; 10-ring zeolite; pore structure; hybrid catalysts.

1. INTRODUCTION

The excellent properties of dimethyl ether (DME) as an eco-friendly substitute for conventional oil-derived diesel fuel [1,2,3] and the need for diversifying energy sources have spurred extensive research in the direct synthesis of DME from syngas as a viable alternative to the traditional two-step process technology. Catalysts employed in the syngas-to-DME process are bifunctional and typically comprise physical mixtures of a Cu-based methanol synthesis catalyst (e.g. Cu-ZnO-Al_2O_3, conveniently abbreviated as CZA) and a solid acid methanol dehydration catalyst, being γ-Al_2O_3 [4,5,6,7] or zeolites [8,9,10,11] the most widely applied. Zeolites are generally admitted to be more suitable than γ-Al_2O_3 as the dehydration component of the bifunctional catalysts because of their stronger acidity enables the direct DME synthesis to be performed at lower reaction temperatures which are thermodynamically more favorable for methanol synthesis [5,12]. As a further advantage, the use of lower temperatures also help in preventing extensive sintering of Cu^0 species which is considered a major source of deactivation in Cu-based methanol synthesis catalysts [5,12].

Given that the Cu-catalyzed methanol synthesis is a long-standing technology, most of the research efforts regarding syngas-to-DME catalysts were devoted to the development of suitable solid acids providing the required methanol dehydration functionality. Improving our understanding on the relationships between the properties of the solid acids and the catalytic performance for direct DME synthesis of the resulting hybrid catalysts or composites is, clearly, of paramount importance for designing more efficient catalysts. In the particular case of zeolites, acidity is consensually admitted to be the most relevant property determining the catalytic behavior of the bifunctional CZA/zeolite catalysts. However, a closer inspection to the related literature reveals significant discrepancies regarding the impact of the density,

type (Brønsted or Lewis), and strength of the acid sites on the activity, selectivity, and stability of the catalysts in the one-step conversion of syngas to DME [5,8,10,13,14,15,16]. Lack of uniformity in both the method of preparation and composition of the catalysts as well as in reaction conditions are likely reasons behind the divergent conclusions reached about the role of zeolite acidity. In many cases, a somewhat incomplete characterization of the zeolite acidity (relying exclusively on NH_3-TPD data) also contributes to the uncertainty [6,8,16,17].

The method by which the two components are combined when preparing the catalysts is expected to impact their catalytic performance in the direct DME synthesis. According to the concept of bifunctionality, catalysts prepared by methods producing a more intimate contact between the metal (Cu) and acid functions are anticipated to perform better in the direct DME synthesis than those leading to a low degree of inter-dispersion between the components. In this line, Zhang et al. [18] have recently reported that hybrid catalysts prepared by the so-called "slurry mixing method" (the zeolite is mixed with the CZA precipitate before it was calcined) were better than those obtained by the "dry-powder method" in which the zeolite is mixed with the CZA component once it is calcined. In that work the authors considered that the "slurry mixing method" was more favorable to inter-dispersion and contact between the copper catalyst and the zeolite and, hence, more efficient for the in situ dehydration of methanol to DME [18]. However, this is not the general case and several examples can be found in the earlier literature where the use of preparation methods favoring a high inter-dispersion of the components does not produce the best catalysts [4,13,19,20,21,22,23]. In our preceding works, we attributed this anomalous behavior to the development of detrimental interactions between the CZA methanol synthesis catalyst and the zeolite in CZA/ZSM-5 hybrid catalysts prepared by the commonly applied method of grinding the powders of

the two components [21,22]. Such interactions were shown to involve a partial exchange of zeolite protons by Cu^{2+} (and possibly Zn^{2+}) species migrated from the CZA catalyst that reduced the density of Brønsted acid sites and, consequently, the methanol dehydration efficiency of the zeolite in the direct DME synthesis [21]. Additionally, the detrimental interactions did also manifest, under conditions where the overall DME synthesis rate is controlled by the methanol synthesis step, in a decline of the CO conversion and DME yield with time caused by a gradual loss of the methanol synthesis activity of the CZA catalyst [22]. Although the origin of the deterioration of the activity with time of the Cu-based catalyst has not yet been elucidated, it is noteworthy that the deactivation rate was significantly influenced by the chemical composition (i.e. nature and concentration of the charge-compensating cations) of the ZSM-5 zeolite [22].

The pore topology is, besides chemical composition, a key design parameter in catalysis by zeolites. In the case of zeolite-based hybrid catalysts for the direct DME synthesis, however, no systematic studies aimed at addressing the influence of the zeolite structure on the final catalytic performance have been so far reported. Indeed, in most of the previous works, ZSM-5 (MFI, 10-ring pore system) has been the zeolite of choice as the methanol dehydration component of the bifunctional catalysts [8,9,13,16,24,25,26,27,28,29,30,31, 32,33]. Besides MFI, other 10-ring pore structures such as FER (ferrierite) [10,14,34] and MWW (MCM-22, MCM-49) [15,35,36] as well as 12-ring pore systems such as FAU (Y) [13,14,37,38,39,40] and MOR (mordenite) [37,41] have also been studied. Unfortunately, any attempt to gather general conclusions regarding topological effects from the aforementioned studies have been discouraging given the disparity in catalyst composition, preparation method, and reaction conditions. Even in the few studies where more than one zeolite structure is compared at equivalent conditions, distinct catalytic behaviors were explained

considering differences in acidity rather than in pore topology [13,14,34,37]. Moreover, in none of the earlier studies was the possibility of a structure-dependent extent of interaction between the Cu catalyst and the zeolite considered as a factor contributing to the observed catalytic performance.

It clearly follows from the above discussions that more systematic studies aimed at addressing the impact of the zeolite pore topology on the catalytic performance of CuZnAl/zeolite hybrid catalysts in the syngas-to-DME process, with special attention to detrimental CZA-zeolite interactions, are particularly timely. To this purpose, in the present work the catalytic performance for the direct DME synthesis of CZA/zeolite hybrid catalysts comprising six 10-ring pore zeolites with different pore structures (ZSM-5, FER, MCM-22, ITQ-2, IM-5, and TNU-9) and similar Si/Al ratio is compared under equivalent conditions. Additionally, the influence of zeolite crystallite size (for ZSM-5) and selective surface dealumination (for MCM-22) is also investigated.

2. EXPERIMENTAL

2.1. Preparation of catalysts

2.1.1. Cu-based methanol synthesis catalyst

The Cu-ZnO-Al_2O_3 methanol synthesis catalyst precursor (nominal Cu:Zn:Al atomic ratio of 6:3:1, abbreviated as CZA) was prepared by coprecipitation from the corresponding metal nitrates as reported elsewhere [22]. Briefly, an aqueous solution of $Cu(NO_3)_2$ (0.6M), $Zn(NO_3)_2$ (0.3M), and $Al(NO_3)_3$ (0.1M) and an aqueous solution of Na_2CO_3 (1M) as precipitating agent were simultaneously added at a rate of 5 cm^3/min to a glass beaker kept under stirring at 70ºC and a pH of 7.0. Afterwards, the suspension was aged for 1 h at this temperature while keeping the pH at 7.0 through the controlled addition of the metal nitrates or sodium carbonate solutions. Then, the resulting

precipitate was filtered, exhaustively washed with deionized water, dried at 100ºC for 12 h, and calcined in flowing air at 300ºC for 3 h.

2.1.2. Zeolites employed as methanol dehydration catalysts

Intentionally, the zeolites selected for this study had an alike bulk Si/Al atomic ratio in the range of 9-14. The samples were either purchased (ZSM-5, FER) or home-synthesized (MCM-22, ITQ-2, IM-5, TNU-9). In the case of ZSM-5, two commercial samples in the ammonium form (TZP322 and TZP302H, TRICAT) with Si/Al ratio of ca. 10 and different crystallite size were employed. The two samples were converted to their H-form by calcination in a muffle oven at 500ºC for 3 h. The produced H-ZSM-5 zeolites were labeled as Z5LC and Z5SC, where LC and SC stand for large and small crystallites, respectively. The same calcination protocol was applied to produce H-ferrierite (denoted as FER) from a commercial NH_4^+-ferrierite sample (CP-914C, Si/Al= 10, Zeolyst).

H-MCM-22 (labeled as M22) was obtained by calcination at 540ºC for 3 h of the layered MCM-22(P) precursor, synthesized from a gel with nominal Si/Al ratio of 15 as detailed in [42]. A portion of the M22 sample was refluxed with a 1.5 M aqueous solution of oxalic acid (99%, Fluka) at 70 ºC for 1.5 h using a liquid-to-solid ratio of 30 cm^3/g. After cooling to room temperature, the solid was filtered, extensively washed with deonized water, dried at 100 ºC, and then calcined in a muffle oven at 500 ºC for 6 h (sample denoted as M22ox). An aliquot of the layered MCM-22(P) precursor was used for the synthesis of the delaminated ITQ-2 zeolite (tagged as ITQ2) according to the procedure reported in [43].

A Na-IM-5 zeolite was hydrothermally synthesized from a gel (SiO_2/Al_2O_3= 35.7 mol/mol) using 1,5-bis(methylpyrrolidinium)pentane dibromide as structure-directing

agent following the procedure described in the original patent [44]. After 14 days of crystallization, the zeolite was recovered by filtration, washed, and calcined at 580ºC in static air for 3 h to remove the organic matter. The protonic form of the zeolite was obtained by submitting the calcined solid to NH_4^+ exchange (80 ºC, 6 h, liquid/solid ratio of 30 cm^3/g) and a final calcination at 500 ºC for 3 h in static air. This sample is denoted as IM5.

TNU-9 zeolite was synthesized by hydrothermal crystallization for around 8 days of a gel with SiO_2/Al_2O_3 mol ratio of 60 using 1,4-dibromobutane and 1-methylpyrrolidine as organic structure-directing agents as reported in [45]. The as-synthesized zeolite was calcined at 580ºC in static air for 3 hours to remove the occluded organic molecules. Then, the H-form of the zeolite (sample denoted as TNU9) was obtained through NH_4^+ exchange and calcination as described before for IM-5.

2.1.3. Preparation of CZA/zeolite hybrid catalysts

Typically, the hybrid catalysts employed in the syngas-to-DME reaction were prepared by carefully grinding in an agate mortar the calcined CZA and zeolite component powders (in a CZA:zeolite mass ratio of 2:1) followed by pelletizing to the 0.25-0.42 mm sieve fraction. The so obtained hybrid catalysts were denoted as CZA/Z, where Z refers to the particular H-zeolite used according to the notation described in the previous section.

An additional series of hybrid catalysts (denoted as CZA+Z) was also prepared using samples Z5SC, FER, and ITQ2 by physically mixing pellets (0.25-0.42 mm sieve fraction) of the CZA and zeolite components in a CZA:zeolite mass ratio of 2:1.

2.2. Characterization techniques

The chemical composition of the samples was determined by inductively coupled plasma-optical emission spectrometry (ICP-OES) in a Varian 715-ES apparatus after dissolution of the solids in an acid mixture of HNO_3:HF:HCl (1:1:3 volume ratio).

Identification of crystalline phases in the CZA oxidic precursor and determination of the phase purity in home-synthesized zeolites (MCM-22, ITQ-2, TNU-9, IM-5) was accomplished by powder X-ray diffraction (XRD). XRD patterns were recorded on a PANanalytical Cubix Pro diffractometer equipped with a graphite monochromator operating at 40 kV and 45 mA using nickel-filtered Cu K_α radiation (λ= 0.1542 nm). The average crystallite size of the CuO phase in calcined CZA and CZA/Z catalysts was estimated by applying the Scherrer's equation to the CuO (111) reflection (2θ= 38.8º).

Textural properties were determined by N_2 adsorption at -196ºC in a Micromeritics ASAP 2000 equipment. The specific surface area was calculated following the BET method and the micropore volume by using the *t*-plot approach. External surface areas (S_{ext}) were obtained by subtracting the micropore area from the BET value. Prior to the adsorption measurements, the samples were degassed at 200ºC (CZA) or 400ºC (zeolites) and vacuum overnight. The lower degassing temperature applied for the CZA component is advised in order to avoid structural changes in the Cu-based catalyst that are reported to occur at temperatures above 300ºC [46].

The average crystal size and the morphology of the zeolites were determined by scanning electron microscopy (SEM) in a JEOL JSM 6300 microscope operated at 30 kV.

The chemical surface analysis of the zeolites was measured by X-ray photoelectron spectroscopy (XPS) in a VG-Escalab-210 spectrometer using the Al Kα radiation (1486.6 eV) and a pass energy of the analyzer of 30 eV.

Solid-state ^{27}Al MAS NMR (magic-angle spinning nuclear magnetic resonance) spectra were recorded at room temperature in a Bruker AV-400 WB spectrometer operating at 104.2 MHz and equipped with a 4 mm Bruker BL4 mm probe. Fully hydrated samples were packed into zirconia rotors and spun at the magic angle spinning (MAS) of 10 kHz. The spectra were acquired with excitation pulses corresponding to a flip angle of $\pi/18$. Chemical shifts were referred to an 0.1 M aqueous solution of $Al(NO_3)_3$.

The reduction behavior for the calcined CZA and CZA/Z catalysts was studied by H_2-TPR in a Micromeritics Autochem 2910 equipment. About 30 mg of sample was initially flushed with Ar at room temperature for 30 min. Then, the gas was switched to the reductive mixture of 10 vol% H_2 in Ar (flow rate = 50 cm^3/min) and the temperature linearly increased from ambient to 600ºC at a heating rate of 10ºC/min. Water formed in the reduction was retained in a 2-propanol/$N_{2(l)}$ trap and the H_2 consumption rate was monitored in a thermal conductivity detector (TCD) previously calibrated using the reduction of CuO as reference.

The total amount of acid sites (Brønsted+Lewis) and the acid strength distribution in the zeolites was determined by NH_3-TPD in an Autochem 2910 equipment (Micromeritics) coupled with a quadrupole mass spectrometer (OmniStar from Balzers Instruments). Prior to ammonia adsorption, ca. 100 mg of sample were pretreated at 450ºC for 30 min in O_2, then in Ar for 15 min, and finally in He for 15 min. Afterwards, the samples were saturated with NH_3 at 175ºC and the chemisorbed ammonia subsequently desorbed by heating from 175ºC to 900ºC at a heating rate of 10ºC/min. The m/z = 16 (NH_2^+) signal in the coupled mass spectrometer was used to obtain the corresponding NH_3 desorption profiles.

The Brønsted acidity of the zeolites was determined by FTIR of adsorbed pyridine. FTIR spectra were recorded in a Nicolet 710 FTIR apparatus for self-supported wafers (10 mg/cm^2) previously pretreated at 400ºC overnight under vacuum of 10^{-2} Pa. Afterwards, $1.8 \cdot 10^3$ Pa of pyridine were admitted to the IR cell and, after equilibration at room temperature (RT), the sample was degassed for 1 h at 250ºC and 400 ºC. After each desorption step the sample was cooled down to RT and the spectra in the pyridine region recorded. Then, the amount of Brønsted acid sites at each desorption temperature was calculated from the integrated area of the band (after background subtraction) at ca. 1545 cm^{-1} using the extinction coefficient reported by Emeis [47]. Additionally, FTIR of adsorbed 2,6-di-*tert*-butyl pyridine (DTBPy) was applied to determine the relative amounts of external Brønsted acid sites by following the stretching band of the protonated amine group (≡N-H$^+$) peaking at ca. 3365 cm^{-1} [48,49]. FTIR-DTBPy measurements were performed in the same equipment used for pyridine on self-supported wafers of ca. 10 mg/cm^2 after pretreatment at 400ºC and vacuum (10^{-2} Pa) overnight. Adsorption of DTBPy was accomplished by equilibrating the wafers with the probe vapor pressure for 12 min at 150ºC, followed by degassing for 1 h at this temperature, and eventually collecting the spectrum at RT.

The total amount of carbon deposits in spent zeolites after their use in methanol dehydration experiments (*vide infra*) was determined by elemental analysis in a Fisons Inst. EA1108 CHNS-O analyzer.

In order to determine the nature of the carbonaceous species, ca. 15 mg of the spent zeolite were dissolved in 1 cm^3 of a concentrated HF aqueous solution (40%, Scharlau) at room temperature. Subsequently, 4 cm^3 of CH_2Cl_2 were added to extract the soluble carbonaceous material which, after its separation from the aqueous phase, was analyzed by GC-MS in an Agilent 6890N gas chromatograph coupled with an Agilent 5973N

Mass Selective Detector (MSD). No insoluble carbon species were found in any of the analyzed spent zeolites.

2.3. Catalytic experiments

2.3.1. Dehydration of methanol

The activity of the zeolites for dehydration of methanol (99.8% purity, Sigma-Aldrich) was determined in a fixed bed continuous-flow quartz reactor loaded with 10-20 mg of zeolite pellets (0.25-0.42 mm) diluted with 2 cm^3 of inert SiC granules (0.6-0.8 mm sieve size). The dehydration experiments were performed at 260ºC (the same reaction temperature applied for the syngas-to-DME experiments, *vide infra*) and atmospheric pressure. Prior to feeding methanol the catalyst was routinely pretreated in situ under flowing nitrogen (60 cm^3/min) at 300ºC for 1 h. Afterwards, the reactor temperature was lowered to 260ºC and the N_2 flow replaced by a mixture of N_2 and MeOH vapor (MeOH:N_2 molar ratio = 20:80, total flow rate 75-150 cm^3/min). For each catalyst, the space velocity was adjusted so as to obtain initial methanol conversions around 50%. The reactor effluent was analyzed at regular time intervals by on line gas chromatography in a HP-GC6890 apparatus equipped with a TBR-5 capillary column and a FID-type detector.

2.3.2. Direct DME synthesis

The syngas-to-DME reactions were performed in a fixed bed stainless steel reactor as detailed in [22]. Typically, the reactor was loaded with 0.7 g of catalyst (0.25-0.42 mm) previously diluted with SiC (0.6-0.8 mm) to attain a total bed volume of 10 cm^3. Prior to reaction the catalyst was in situ reduced by flowing 120 cm^3/min of diluted hydrogen (5 vol% H_2 in N_2) through the reactor at atmospheric pressure and 245 ºC

(2ºC/min) for 10 h. Afterwards, the temperature of the catalyst bed was lowered to 85ºC under the flow of diluted H_2 and the reductive gas replaced by a mixture of 90 vol% syngas/10 vol% Ar (Ar used as internal standard for GC analyses) with the syngas having the molar composition of 66%H_2/30%CO/4%CO_2. Then, the reaction conditions of 4.0 MPa total pressure and 260ºC temperature were established and the flow rate of the feed gas mixture (syngas/Ar) adjusted to obtain a space velocity of 1700 $cm^3_{syngas}/(g_{cat} \cdot h)$.

The product stream leaving the reactor was analyzed on line in a Varian 450-GC gas chromatograph equipped with a TCD and a FID. Product selectivities are given on a carbon basis. The selectivity to CO_2 was calculated taking into account the amount of CO_2 contained in the feed. Carbon mass balances for the reported syngas-to-DME experiments were closed 100 ± 2%.

3. RESULTS AND DISCUSSION

3.1. Characterization of materials

3.1.1. Physicochemical properties of the Cu-ZnO-Al_2O_3 (CZA) catalyst

The XRD pattern of the calcined CZA precursor (not shown) presents the characteristic diffractions for CuO and ZnO phases, with a mean CuO crystallite size of 5.4 nm. The BET surface area of the material as measured by N_2 sorption is 98 m^2/g. The reduction profile of this sample obtained by H_2-TPR features a main reduction peak at T_{max}= 205ºC and evidences complete reduction of CuO to Cu^0 at temperatures well below that of the in situ H_2-reduction treatment applied prior to catalysis (245ºC). Further details on the physicochemical properties of the CZA oxide precursor can be found in [22].

3.1.2. Physicochemical properties of the zeolites

The X-ray diffraction (XRD) patterns for the H-zeolites are given in Fig. 1. All the home-made zeolites (MCM-22, ITQ-2, IM-5, TNU-9) exclusively display the reflections characteristic for their respective crystalline structures, confirming the high purity of the synthesized materials.

The chemical compositions as well as the main morphological and textural properties of the zeolites are summarized in Table 1. With the exception of TNU9 (*vide infra*), the bulk Si/Al ratios determined with ICP-OES are in good agreement with those expected according to the suppliers or synthesis gels. The slightly higher bulk Si/Al ratio observed for ITQ2 (12.2) as compared to M22 (10.5) is indicative of a certain dealumination occurring at the acidic conditions (pH< 2) applied for separation of the layers during its preparation [50,51]. Expectedly, treatment of M22 with oxalic acid (M22ox) increased the bulk Si/Al ratio from 10.5 to 13.9 due to partial dealumination of the zeolite. In the case of TNU9, a Si/Al ratio of 13.5 is obtained for the calcined zeolite. The fact that this value is significantly lower than that used in the synthesis gel (Si/Al= 30) is a consequence of a lower degree of incorporation of Si with respect to Al from the solution to the final zeolite.

A nearly uniform Al distribution through the crystallites for most of the studied zeolites is inferred at the view of the similar bulk and surface (from XPS analysis) Si/Al ratios (Table 1). Exceptions to this observation are TNU-9 and, expectedly, the MCM-22 zeolite treated with oxalic acid (M22ox). For TNU-9, the slightly higher surface Si/Al ratio (17.9) as compared to the bulk (13.5) is suggestive of a preferential incorporation of Si to the solid at the late stages of the crystallization process once most of the Al precursor in the reaction medium has been consumed. In turn, the comparison of the bulk and surface Si/Al ratios for samples M22 (12.1) and M22ox (20.0) points

toward a preferential dealumination of the external zeolite surface during the treatment with oxalic acid, in agreement with earlier observations [52,53,54].

The morphology and mean size of the zeolite crystallites as obtained by SEM are also presented in Table 1. In agreement with the specifications provided by the supplier, the average crystallite size of sample Z5LC featuring a parallelepiped morphology was about one order of magnitude larger than that of the spherical-shaped crystallites of Z5SC. M22 and ITQ2 crystallites featured the expected thin-plate (or platelet) morphology [53,55] with dimensions of ca. 860x80 nm and 740x100 nm, respectively. IM5 and TNU9 crystallites also displayed a parallelepiped-like morphology sizing, respectively, 710x250x250 nm and 550x270x140 nm. Representative SEM images for the studied zeolites are provided in Fig. S1 of *Supplementary Material*.

Textural properties derived from N_2 adsorption measurements are also shown in Table 1. Sample Z5SC displays a nearly 4-fold higher external surface area (S_{ext}= 39 m^2/g) than Z5LC (S_{ext}= 11 m^2/g), as anticipated from the smaller crystallite size of the former. In turn, ITQ-2 expectedly exhibits a significantly larger external surface area (324 m^2/g) than MCM-22 (88 m^2/g). It is also seen that treatment of M22 with oxalic acid (M22ox) preserves the integrity of the MCM-22 structure. Finally, IM5 and TNU9 display equivalent external surface areas (12 m^2/g) concurring with their alike crystallite size and morphology.

The ^{27}Al MAS NMR spectra of the hydrated H-zeolites are depicted in Fig. 2. All samples feature a main peak at δ= 52-55 ppm attributed to tetrahedral Al species (Al^{IV}) in the zeolite lattice. This band is notably broader for M22 and ITQ2 samples, for which additional Al^{IV} signals at ca. 61 and 50 ppm are discerned. Previous studies have assigned these additional Al^{IV} resonances in MCM-22 and the topologically related MCM-49 zeolites to tetrahedral Al species occupying distinct T sites in the zeolite

framework [56,57,58]. Besides, an additional peak at around 0 ppm assigned to hexacoordinated extraframework Al (EFAL) species (Al^{VI}) is evidenced in all zeolites. The lowest relative proportion of EFAL is estimated for Z5LC, Z5SC, FER, and IM5 (~10%) while M22 and ITQ2 display the highest relative concentration of EFAL (~20%), with TNU9 exhibiting an intermediate behavior (~15%). Furthermore, the treatment of M22 with oxalic acid does not substantially modify the average coordination of Al species, despite the observed changes in both bulk and surface Si/Al ratios (Table 1). This suggests that, at the conditions applied, oxalic acid removes both framework and extraframework Al species [35] with no apparent preference for one type over the other.

The NH_3 uptakes at 175ºC and the corresponding NH_3-TPD profiles are shown in Table 2 and Fig. 3, respectively. According to these values, the total amount of acid sites (Brønsted+Lewis) decreases in the following order: M22 > IM5 > FER ≥ TNU9 > Z5LC ≥ M22ox > Z5SC > ITQ2. Expectedly, this trend does not show a clear correlation with the total Al content in the zeolites due, at least in part, to differences in the amount and nature of EFAL species as previously discussed on the basis of ^{27}Al MAS NMR. Nonetheless, some general trends can be evidenced from the obtained NH_3 uptakes: a) ZSM-5 with large crystallites (Z5LC) has more total acid sites than its low crystallite size counterpart (Z5SC), b) treatment of M22 with oxalic acid reduces the total amount of acid sites, and c) ITQ2 has a lower amount of acid sites than M22.

As seen in Fig. 3, all zeolites show a main desorption feature with T_{max} in the temperature range of ca. 320-405ºC related to strong acid sites along with a shoulder at lower temperatures (in the 200-300ºC range) ascribed to acid sites of weak-medium strength. T_{max} values for the main desorption peak are given in Table 2. Taking the T_{max} value as an estimation of the average acid strength [59], the following decreasing order

is found: FER ≥ TNU9 > M22ox > IM5 ≥ Z5LC > Z5SC ≥ M22 > ITQ2. Thus, FER and TNU9 bear the strongest acid sites while ITQ2 and M22 are at the opposite extreme, with IM5 and Z5LC having an intermediate acid strength. The higher average acid strength of Z5LC as compared to Z5SC has been related to a lower strength of the acid sites residing on the external surface [60]. This fact may also account for the lower acid strength of ITQ-2 zeolite as compared to MCM-22 [50,53,61]. Following this reasoning, the observed increase in T_{max} from 341 to 385ºC upon treatment of M22 with oxalic acid M22ox (385ºC) can be accounted for by the preferential removal of weaker acid sites associated to Al species on the external zeolite surface.

The concentrations of Brønsted acid sites (BAS) measured by FTIR-pyridine after desorbing the base at 250ºC and 400ºC are included in Table 2. The comparatively low amount of BAS detected by pyridine after desorption at 250ºC for the FER sample contrasts with its relatively high NH_3 uptake (Table 2). This fact has been attributed to a restricted access of pyridine molecules to part of the acid sites in the FER structure, most likely those located inside the ferrierite cavity at the intersection of the 6- and 8-ring channels [62,63]. Regarding the rest of samples, IM5, TNU9, Z5LC, and Z5SC possess more BAS (both at 250ºC and 400ºC) than M22 and ITQ2. Comparatively, the BAS in ITQ2 display the lowest average strength, which can be related to the lower strength of the external acid sites, as discussed previously. As observed in Table 2, the ZSM-5 sample with larger crystallites shows a higher amount of BAS than the small crystal size analogue whatever the pyridine desorption temperature.

Finally, the relative concentration of BAS located on the external surface of the studied zeolites is compared in Table 2 based on the intensity (in arbitrary units) of the 3365 cm^{-1} IR band of protonated DTBPy. As seen in Table 2, ITQ2 possesses the largest amount of external BAS, followed by M22. Notice that these two samples

display, by large, the largest external surface areas (Table 1). In turn, the surface Brønsted acidity is reduced by about 34% after the treatment of M22 with oxalic acid as a consequence of the preferential surface dealumination (Table 1). A much lower relative amount of external BAS is observed for the rest of zeolites, and particularly for the ZSM-5 sample with larger crystallites (Z5LC) and IM5.

3.1.3. Properties of Cu species in CZA/zeolite hybrid catalysts

According to XRD characterization, the grinding method applied for the preparation of the CZA/zeolite hybrid catalysts does not produce any appreciable change in the nature and mean size of the crystalline CuO phase in the CZA component with respect to the bare CZA catalyst. This is exemplified for the CZA/ITQ2 hybrid in Fig. S2 of *Supplementary Material* by comparing the experimentally obtained XRD pattern with that simulated from the patterns of the individual CZA and ITQ2 components considering a CZA:ITQ2 mass ratio of 2:1.

Additionally, the reduction behavior of the hybrid catalysts was studied by H_2-TPR. The corresponding reduction profiles are shown in Fig. 4. It can be seen that all the samples feature similar reduction behaviors, with a main reduction peak (T_{max}) associated to the reduction of CuO to metallic Cu centered in the short temperature interval of 200-210ºC. These T_{max} values are very close to the value of 205ºC obtained for the bare CZA catalyst (see section 3.1.1), indicating that no major changes in the reduction properties of CuO species in the CZA component have occurred at the grinding stage. It can be seen in Fig. 4, however, that the temperature window for the reduction of CuO species varies to some extent depending on the particular zeolite. Since XRD data did not show appreciable changes in the average CuO particle size for the hybrid catalysts with respect to the bare CZA catalyst, as previously discussed,

small variations in the reducibility of CuO species probably reflect subtle modifications in the interaction strength of this oxide with the zeolite [13,34,64]. As qualitatively appreciated in Fig. 4, the reduction interval appears to broaden for the catalysts comprising zeolites with relatively large external surface areas such as ITQ2, M22, and the small crystal size Z5SC sample (Table 1). Moreover, it is inferred from the comparison of the reduction profiles for CZA/M22 and CZA/M22ox that preferential removal of Al species from the external zeolite surface reduces the temperature window for CuO reduction.

Thus, grinding of the CZA and the zeolite powders at the catalyst preparation stage appears to induce subtle modifications in the strength of the interaction between this oxide and the zeolite. In turn, the heterogeneity of the CuO-zeolite interaction strength appears to increase with the amount of Al species on the external zeolite surface which may come in contact with the CZA component during the grinding process.

3.2. Catalytic experiments

3.2.1. Catalytic behavior of zeolites in methanol dehydration

Prior to assessing the catalytic behavior of the hybrid catalysts in the direct DME synthesis, the zeolites were evaluated for the dehydration of pure methanol at the same reaction temperature employed in the syngas-to-DME experiments (260ºC). Under the applied conditions, all zeolites produced DME with selectivity above 99.5% (on a carbon basis). To avoid any interference from deactivation issues (*vide infra*), the activity of the zeolites will be discussed in terms on initial methanol dehydration rates (extrapolated at TOS= 0 from the rate-TOS curves, see Fig. S3 of *Supplementary Material*). According to the initial rates, the activity for methanol dehydration decreases in the following order (rates given in parenthesis as $\mu mol \cdot (g_{zeol} \cdot s)^{-1}$): FER (1017) >

Z5LC (908) > Z5SC (841) > IM5 (675) > TNU9 (608) > M22 (542) > M22ox (458) > ITQ2 (417). In a previous work, we found a linear correspondence between the amount of strong BAS determined by FTIR-pyridine at a desorption temperature of 400ºC (B400) and the initial methanol dehydration rate for an extended series of ZSM-5 samples with different acidic properties [22]. In the present study, a good linear relationship between the initial rates and B400 has also been found for the series of zeolites studied, provided FER is excluded from the correlation (Fig. 5). The fact that the activity of FER does not follow the correlation can be related to the underestimation of the amount of BAS from FTIR-pyridine measurements, as discussed in 3.1.2. Worse linear correlation coefficients were obtained when the initial rates are plotted against the total (Brønsted+Lewis) amount of acid sites (given by the NH_3 uptakes) or the density of BAS measured by FTIR-pyridine after desorbing the base at 250ºC (B250), as shown in Fig. S4 of *Supplementary Material*. Therefore, it can be stated that the methanol dehydration activity (in the absence of deactivation phenomena) in the studied zeolites is mostly dictated by the density of strong Brønsted acid sites rather than by the pore topology.

It is evident from the rate-TOS curves given in Fig. S3 that all zeolites experience a gradual loss of activity during the methanol dehydration experiments at the studied conditions. For a better comparison of the deactivation trends, the relative reaction rates (calculated as r_t/r_0, where r_t and r_0 are, respectively, the rates at TOS=t and TOS=0) are presented in Fig. 6. As seen there, the deactivation rate increases from FER (the most stable) to M22ox (the less stable) in the following order: FER < Z5LC < IM5 ~ Z5SC < TNU9 < ITQ2 < M22 < M22ox. The first observation one can make from this trend is that there is no obvious relationship between the extent of deactivation and the amount and/or strength of the zeolite acid sites. The loss of activity observed during the

methanol dehydration experiments is attributed to the formation of carbonaceous deposits originated from DME probably via the intermediate formation of light olefins as it is believed to occur, thought much more severely, in the methanol-to-hydrocarbons (MTH) process [65].

The amount of carbon present in the spent zeolites was determined by elemental analysis. Even if there is a certain correlation between the total amount of carbon and the relative loss of activity during the methanol dehydration experiments (Fig. 7), it is clear that this parameter alone does not provide a full explanation for the observed trends. In order to better understand the deactivation behavior of the zeolites, the nature of the carbonaceous species formed was assessed by GC-MS analysis of the organic matter previous dissolution of the spent zeolites in concentrated HF (see section 2.2).

The species detected by GC-MS comprised the following general families of hydrocarbons: long-chain linear and branched (mostly methyl) aliphatics, polymethylated benzenes, 2- and 3-ring alkylated olefinic naphthenes, and 2- and 3-ring alkylated aromatics. Thought practically all these types of species were found in all spent zeolites, the predominant carbon structures varied depending on the particular zeolite: aliphatics in FER, aliphatics and penta- and hexa-methyl benzenes in Z5LC and Z5SC, polyalkylated benzenes and alkylated 2-ring naphthenes in IM5 and TNU9, and 2- and 3-ring alkylated naphthenes and aromatics in M22, M22ox, and ITQ2. This shows that the formation of cyclic structures, which generally induce a higher deactivating effect in zeolites [66], becomes strongly hindered in the 8- and 10-ring pores of FER. The low carbon content and almost absence of cyclic carbon species may account for the higher stability of FER during methanol dehydration (Fig. 6). The size of the 10-ring pores in ZSM-5 is large enough to allow for the formation of alkylated benzenes but it imposes serious spatial restrictions for accommodating bulkier multi-

ring compounds. In fact, cationic derivatives of methylated benzenes are believed to be active sites in the conversion of methanol to hydrocarbons over HZSM-5 according to the so-called "hydrocarbon pool" mechanism [67,68]. It is worth noting that, besides aliphatics and alkylbenzenes, 2-ring cyclic structures were also detected (though in much lower concentrations) in the small crystal size Z5SC sample, suggesting that they were probably formed at the unconstrained external acid sites. Thus, the higher total amount of carbonaceous deposits and the formation of somewhat heavier carbon species is the likely cause for the observed higher deactivation of Z5SC as compared to Z5LC.

On the other hand, the formation of a higher amount and bulkier alkylated 2-ring carbon structures in IM-5 and TNU-9 as compared to ZSM-5 can be related to the particular and more complex pore connectivity of the former. In TNU-9, the presence of large 12-ring cavities of about 0.72 nm in diameter formed at the intersection of the two 10-ring channel systems allows the accommodation of bulkier molecules than in ZSM-5. Indeed, TNU-9 has been shown to behave like a 12-ring zeolite in the disproportionation of toluene [45]. Similarly, the highly interconnected 2D 10-ring pore system of IM-5 [69] gives it the character of a multidimensional channel system with less steric constraints than ZSM-5 in hydrocarbon conversion reactions [70,71]. These peculiar structural features make carbon species in IM-5 and TNU-9, even if being somewhat bulkier, to produce a lower deactivating effect than in ZSM-5 during methanol dehydration. Indeed, these zeolites showed similar relative losses of activity (30-40%, Fig. 7) despite the total amount of carbon accumulated was significantly higher in TNU9 (ca. 5 wt%) and IM5 (ca. 3.5 wt%) than in Z5SC and Z5LC (1.3-1.7 wt%).

Moreover, M22 and ITQ2 samples having less constrained pore structures are those displaying both higher carbon contents and higher relative deactivation rates during the

dehydration of methanol (Fig. 7). A significant part of the carbon species in these zeolites contained polyalkylated 2- and 3-ring cyclic structures which probably formed on the acid sites located at the external 12-ring pockets as well as in the 12-ring supercages (sizing 0.71x0.71x1.84 nm) accessible through relatively small 10-ring windows (0.40x0.55 nm). Indeed, formation of such alkylated multi-ring carbonaceous species inside the sinusoidal 10-ring channels seems unlikely [72]. The fact that, despite their similar carbon content, M22ox (with a lower external acidity) experiences a higher deactivation than M22 suggests that carbon species trapped in the 12-ring supercages have a higher deactivating character than those located on the external 12-ring pockets.

It can be concluded from the above results that, contrary to the catalytic activity, the deactivation behavior of zeolites during methanol dehydration is mostly dictated by their pore structure, which determines the amount and nature of the formed carbon species, rather than by their acidic properties.

3.2.2. Direct DME synthesis on CZA/zeolite hybrid catalysts

CZA/zeolite hybrid catalysts prepared by grinding the individual component powders in a CZA:zeolite mass ratio of 2:1 (see section 2.1.3) were evaluated for the direct DME synthesis at 260ºC, 4.0 MPa, space velocity of 1700 $cm^3/(g_{cat} \cdot h)$, and a total time-on-stream (TOS) of ca. 50 h. Under these conditions all the catalysts displayed an alike and constant selectivity pattern (63-65% DME, 3-5% MeOH, 30-32% CO_2, and <1% hydrocarbons, in %C) which approaches that predicted by the thermodynamic equilibrium at the studied conditions (68% DME, 5% MeOH, 27% CO_2), as seen in Fig. S5 of *Supplementary Material*. This result indicates that all the hybrid catalysts bear an "excess" of active acid sites so as to rapidly dehydrate in situ the methanol formed on the CZA catalyst to its near-equilibrium value. In other words, under the studied

conditions the overall rate of CO conversion (and DME formation) from syngas is controlled by the rate of methanol synthesis. The invariability of the selectivities with TOS evidences that this holds true for the entire experiment.

Unlike selectivities, the catalysts experienced a progressive and disparate decline in CO conversion with TOS, despite their alike "initial" (TOS< 10 h) CO conversions (Fig. 8). The later observation is consistent with the similar properties of the CZA component in the different CZA/zeolite catalysts after the grinding process, as discussed in section 3.1.3. The relative loss of conversion after ca. 50 h on stream increased from ca. 3% for CZA/TNU9 to ca. 16% for CZA/ITQ2 in the following order (only the zeolite component is mentioned): TNU9 < M22ox < IM5 < Z5LC < FER < Z5SC < M22 < ITQ2. Since, as demonstrated before, the overall DME synthesis process is governed by the methanol synthesis step, it is clear that the observed decrease in CO conversion is the consequence of a gradual loss of activity of the CZA catalyst. Indeed, there is no obvious relationship between the deactivation trend of the zeolites in methanol dehydration and that of the hybrid catalysts in the one-step DME synthesis (Fig. S6 of *Supplementary Material*). In a previous study, we observed a similar deactivation behavior for CZA/ZSM-5 hybrid catalysts prepared by grinding comprising ZSM-5 samples with different acid properties [22]. The deactivation during the syngas-to-DME reaction was attributed to detrimental CZA-zeolite interactions that develop when both components are in close contact one to each other, as in the hybrid catalysts obtained by grinding. This seems to be also the case for the catalysts studied here as no significant deactivation (relative loss of CO conversion after ca. 50 h below 1%) was observed for equivalent catalysts prepared as physical mixtures of the pre-pelletized components, as seen in Fig. S7 of *Supplementary Material*. In line with this result, Bonura et al. [23] have recently reported a superior performance in the direct CO_2

conversion to DME for a Cu-ZnO-ZrO_2/HZSM-5 hybrid catalyst prepared by physical mixing of pre-pelletized components with respect to that prepared by grinding of the powdered single components.

At first sight, two main general observations can be made at the view of the deactivation trends depicted in Fig. 8: a) the extent of deactivation is higher for catalysts comprising zeolites with large external surface areas (S_{ext}), such as ITQ2 and M22, and b) preferential removal of Al species from the surface of M22 by oxalic acid treatment significantly improves the stability of the hybrid catalyst. In order to decouple the contribution of these two parameters, the relative decrease in CO conversion after ca. 50 h on stream ($-\Delta X_{CO}$) has been plotted against S_{ext} for two groups of samples with equivalent surface compositions (Fig. 9a), and against the surface Al concentration (given as the atomic Al/(Si+Al) ratio obtained by XPS) for two groups of zeolites with alike S_{ext} values (Fig. 9b). In this later case, it is apparent that the increase in the extent of deactivation with the surface Al content not only holds true for the couple M22-M22ox sharing the same structural features but also for zeolites with distinct topologies (TNU9, IM5, FER, Z5LC).

In order to gather both parameters into a single one, a parameter α has been arbitrarily defined here $\alpha = [Al/(Si+Al)]_{XPS} \cdot S_{ext}$. As seen in Fig. 10, a reasonably good non-linear correlation between the relative extent of deactivation of the hybrid catalysts and α is perceived. This trend clearly indicates that it is the combination of the external surface area and the increasing surface Al concentration in the zeolite what largely determines the extent of the detrimental interactions between the zeolite and the CZA catalyst and, consequently, the deactivation of the catalysts. According to this, zeolites featuring both a low external surface area and high surface Si/Al ratio will minimize detrimental CZA-zeolite interactions and, thus, will produce more stable hybrid

catalysts during the direct DME synthesis. In the present study, this behavior is exemplified by zeolite TNU-9. At the opposite extreme, zeolites like ITQ-2 having high external surface area and Al-rich surface are less suitable as the methanol dehydration function in hybrid catalysts prepared by the generally applied method of grinding.

Considering the above results, it can be suggested that the detrimental interactions causing a gradual loss of the methanol synthesis activity of the Cu species during the syngas-to-DME reaction could be related to interactions of zeolitic Al species with Cu sites at the surface-contact between the zeolite and CZA particles in the hybrid catalyst. Nevertheless, further studies are required in order to elucidate the mechanism by which such detrimental interactions occur as well as to shed more light into the nature of the Al species involved in the interactions.

4. CONCLUSIONS

In this work six 10-ring pore H-zeolites (ZSM-5, FER, IM-5, TNU-9, MCM-22, ITQ-2) with similar bulk Si/Al ratios were studied in order to assess the impact of the pore structure on their catalytic performance for methanol dehydration as well as the behavior of bifunctional CZA/zeolite catalysts in the one-step conversion of syngas to DME. In addition, the influence of crystallite size in ZSM-5 and selective surface dealumination by treatment of MCM-22 with oxalic acid was also investigated. The studied zeolites presented distinct activities and deactivation behaviors in the dehydration of methanol. The initial dehydration activity was structure-independent and became mostly dictated by the density of strong Brønsted acid sites (as measured by FTIR-pyridine after desorbing the base at 400ºC). By contrast, the extent of deactivation during methanol dehydration was driven by the zeolite pore architecture which determined, to a great extent, the amount and nature of the carbon deposits.

Furthermore, decreasing the crystallite size of ZSM-5 and reducing the surface acidity of MCM-22 by treatment with oxalic acid increased the extent of deactivation in methanol dehydration.

Hybrid CZA/zeolite catalysts prepared by grinding the two component powders in a CZA:zeolite mass ratio of 2:1 were evaluated for syngas-to-DME under kinetic control by the Cu-catalyzed methanol synthesis reaction. Under these conditions a progressive decline with TOS (up to ca. 50 h) of the CO conversion (and DME yield) was observed for all the hybrid catalysts, reflecting a gradual deactivation of the Cu sites in CZA active for methanol synthesis. The extent of deactivation increased with increasing the external surface area and the surface Al concentration of the zeolite co-catalyst. These results suggest that the detrimental interactions causing a progressive loss of activity of the Cu-based catalyst are promoted by zeolitic Al species located at the boundary between the CZA and zeolite particles.

As a general conclusion it can be stated that, for CZA/zeolite hybrid catalysts obtained by the commonly applied grinding method, the use as methanol dehydration function of zeolites combining low external surface areas (i.e. large crystallites) and Al-depleted external surfaces is advantageous in order to minimize detrimental interactions and, hence, to extend the catalyst lifetime during the syngas-to-DME process.

Acknowledgments

Financial support by the Comisión Interministerial de Ciencia y Tecnología (CICYT) of Spain through the Project CTQ2010-17988/PPQ is gratefully acknowledged. A. García-Trenco thanks the Ministerio de Economía y Competitividad (former Ministerio de Ciencia e Innovación) of Spain for a predoctoral (FPI) scholarship.

References

[1] T.A. Semelsberger, R.L. Borup, H.L. Greene, J. Power Sources 156 (2006) 497-511.

[2] N. Inoue, Y. Ohno, Petrotech 24 (2001) 319-322.

[3] C. Arcoumanis, C. Bae, R. Crookes, E. Kinoshita, Fuel 87 (2008) 1014-1030.

[4] J.L. Li, X.G. Zhang, T. Inui, Appl. Catal. A 147(1996) 23-33.

[5] T. Takeguchi, K. Yanagisawa, T. Inui, M. Inoue, Appl. Catal. A 192 (2000) 201-209.

[6] D. Mao, W. Yang, J. Xia, B. Zhang, G. Lu, J. Mol. Catal. A 250(2006) 138-144.

[7] I. Sierra, J. Ereña, A.T. Aguayo, J.M. Arandes, J. Bilbao, Appl. Catal. B 94 (2010) 108-116.

[8] J.-H. Kim, M.J. Park, S.J. Kim, O.-S. Joo, K.-D Jung, Appl. Catal. A 264 (2004) 37-41.

[9] D. Mao, W. Yang, J. Xia, B. Zhang, Q. Song, Q. Chen, J. Catal. 230 (2005) 140-149.

[10] J.W. Bae, S.-H. Kang, Y-.J. Lee, K.-W. Jun, Appl. Catal. B 90 (2009) 426-435.

[11] N. Khandan, M. Kazemeini, M. Aghaziarati, Appl. Catal. A 349 (2008) 6-12.

[12] M. Xu, J.H. Lunsford, D.W. Goodman, A. Bhattacharyya, Appl. Catal. A 149 (1997) 289-301.

[13] Q. Ge, Y. Huang, F. Qiu, S. Li, Appl. Catal. A 167 (1998) 23-30.

[14] S.H. Kang, J.W. Bae, K.W. Jun, H.S. Potdar, Catal. Comm. 9 (2008) 2035-2039.

[15] D. Mao, J. Xia, Q. Chen, G. Lu, Catal. Comm. 10 (2009) 620-624.

[16] L. Wang, Y. Qi, Y. Wei, D. Fang, S. Meng, Z. Liu, Catal. Lett. 106 (2006) 61-66.

[17] J. Xia, D. Mao, B. Zhang, Q. Chen, Y. Tang, Catal. Lett. 98 (2004) 235-240.

[18] M.-H. Zhang, Z.-M. Liu, G.-D. Lin, H.-B. Zhang, Appl. Catal. A 451 (2013) 28-35.

[19] G.R. Moradi, S. Nosrati, F. Yaripor, Catal. Commun. 8 (2007) 598-606.

[20] S.P. Naik, H. Du, H. Wan, V. Bui, J.D. Miller, W.W. Zmierczak, Ind. Eng. Chem. Res. 47 (2008) 9791-9794.

[21] A. García-Trenco, A. Vidal-Moya, A. Martínez, Catal. Today 179 (1) (2012) 43-51.

[22] A. García-Trenco, A. Martínez, Appl. Catal. A 411-412 (2012) 170-179.

[23] G. Bonura, M. Cordaro, L. Spadaro, C. Cannilla, F. Arena, F. Frusteri, Appl. Catal. B 140-141 (2013) 16-24.

[24] M. Jia, W. Li, H. Xu, S. Hou, Q. Ge, Appl. Catal. A 233 (2002) 7-12.

[25] K. Sun, W. Lu, F. Qiu, S. Liu, X. Xu, Appl. Catal. A 252 (2003) 243-249.

[26] G. Yang, N. Tsubaki, J. Shamoto, Y. Yoneyama, Y. Zhang, J. Am. Chem. Soc. 132 (2010) 8129-8136.

[27] Y. Luan, H. Xu, C. Yu, W. Li, S. Hou, Catal. Lett. 125 (2008) 271-276.

[28] A.T. Aguayo, J. Ereña, I. Sierra, M. Olazar, J. Bilbao, Catal. Today 106 (2005) 265-270.

[29] J. Ereña, R. Garoña, J.M. Arandes, A.T. Aguayo, J. Bilbao, Catal. Today 107-108 (2005) 467-473.

[30] Y. Luan, H. Xu, C. Yu, W. Li, S. Hou, Catal. Lett. 115 (2007) 23-26.

[31] Y. Lv, T. Wang, C. Wu, L. Ma, Y. Zhou, Biotechnol. Adv. 27 (2009) 551-554.

[32] F.S.R. Barbosa, V.S.O. Ruiz, J.L.F. Monteiro, R.R. de Avillez, L.E.P. Borges, L.G. Appel, Catal. Lett. 126 (2008) 173-178.

[33] G. Moradi, J. Ahmadpur, M. Nazari, F. Yaripur, Ind. Eng. Chem. Res. 47 (2008) 7672-7679.

[34] P.S.S. Prasad, J.W. Bae, S.-H. Kang, Y.-J. Lee, K.-W. Jun, Fuel Process. Technol. 89 (2008) 1281-1286.

[35] J. Xia, D. Mao, W. Tao, Q. Chen, Y. Zhang, Y. Tang, Microp. Mesop. Mater. 91 (2006) 33-39.

[36] J. Xia, D. Mao, N. Xu, Q. Chen, Y. Zhang, Y. Tang, Chem. Lett. 33 (2004) 1456-1457.

[37] A.C. Sofianos, M.S. Scurrell, Ind. Eng. Chem. Res. 30 (1991) 2372-2378.

[38] J.-H. Fei, X.-J. Tang, Z.-Y. Huo, H. Lou, X.-M. Zheng, Catal. Commun. 7 (2006) 827-831.

[39] J. Fei, Z. Hou, B. Zhu, H. Lou, X. Zheng, Appl. Catal. A 304 (2006) 49-54.

[40] D. Jin, B. Zhu, Z. Hou, J. Fei, H. Lou, X. Zheng, Fuel 86 (2707-2713.

[41] N. Khandan, M. Kazemeini, M. Aghaziarati, Catal. Lett. 129 (2009) 111-118.

[42] A. Corma, C. Corell, J. Pérez-Pariente, Zeolites 15 (1995) 2-8.

[43] A. Corma, V. Fornés, S.B. Pergher, Th.L.M Maesen, J.G. Buglas, Nature 396 (1998) 353.

[44] E. Benazzi, J.L. Guth, L. Rouleau, WO 98/17581, 1998.

[45] S.B. Hong, H.K. Min, C.-H. Shin, P.A. Cox, S.J. Warrender, P.A. Wright, J. Am. Chem.Soc. 129 (2007) 10870–10885.

[46] C. Baltes, S. Vukojević, F. Schüth, J. Catal. 258 (2008) 334-344

[47] C.A. Emeis, J. Catal. 141 (1993) 347-354.

[48] A. Corma, V. Fornés, L. Forni, F. Márquez, J. Martínez-Triguero, D. Moscotti, J. Catal. 179 (1998) 451-458.

[49] A. Corma, U. Diaz, V. Fornés, J.M. Guil, J. Martínez-Triguero, E.J. Creyghton, J. Catal. 191 (2000) 218–224.

[50] H.J. Jung, S.S. Park, C.-H. Shin, Y.-K. Park, S.B. Hong, J. Catal. 245 (2007) 65-74.

[51] A. Martínez, S. Valencia, R. Murciano, H.S. Cerqueira, A.F. Costa, E.S. S.-Aguiar, Appl. Catal. A 346 (2008) 117-125.

[52] X. Ren, J. Liang, J. Wang, J. Porous Mater. 13 (2006) 353–357.

[53] H.-K. Min, M.B. Park, S.B. Hong, J. Catal. 271 (2010) 186-194.

[54] S.-H. Lee, C.H. Shin, S.B. Hong, J. Catal. 223 (2004) 200-211.

[55] C. Delitala, M.D. Alba, A.I. Becerro, D. Delpiano, D. Meloni, E. Musu, I. Ferino, Microp. Mesop. Mater. 118 (2009) 1-10.

[56] S.L. Lawton, A.S. Fung, G.J. Kennedy, L.B. Alemany, C.D. Chang, G.H. Hatzikos, D.N. Lissy, M.K. Rubin, H.K.C. Timken, S. Steuernagel, D.E. Woessner, J. Phys. Chem. 100 (1996) 3788-3798.

[57] M. Hunger, S. Ernst, J. Weitkamp, Zeolites 15 (1995) 188-192.

[58] W. Kolodziejski, C. Zicovich-Wilson, C. Corell, J. Perez-Pariente, A. Corma, J. Phys. Chem. 99 (1995) 7002-7008.

[59] R. Ramos Pinto, P. Borges, M.A.N.D.A. Lemos, F. Lemos, J.C. Védrine, E.G. Derouane, F. Ramôa Ribeiro, Appl. Catal. A 284 (2005) 39-46.

[60] K. Kim, R. Ryoo, H.-D. Jang, M. Choi, J. Catal. 288 (2012) 115-123.

[61] B. Onida, L. Borello, B. Bonelli, F. Geobaldo, E. Garrone, J. Catal. 214 (2003) 191-199.

[62] B. Witcherlová, Z. Tvarůžkovà, Z. Sobalík, P. Sarv, Microp. Mesop. Mater. 24 (1998) 223-233.

[63] A.B. Pinar, C. Márquez-Álvarez, M. Grande-Casas, J. Pérez-Pariente, J. Catal. 263 (2008) 258-265.

[64] G.R. Moradi, S. Nazari, F. Yaripor, Fuel Process. Technol. 89 (2008) 1287-1296.

[65] M. Stöcker, Microp. Mesop. Mater. 29 (1999) 3-48.

[66] M. Guisnet, P. Magnoux, Appl. Catal. A 212 (2001) 83-96.

[67] M. Bjorgen, U. Olsbye, D. Petersen, S. Kolboe, J. Catal. 221 (2004) 1-10.

[68] B. Arstad, S. Kolboe, J. Am. Chem. Soc. 123 (2001) 8137-8138.

[69] C. Baerlocher, F. Gramm, L. Massüger, L.B. McCusker, Z. He, S. Hovmöller, X. Zou, Science 315 (2007) 1113-1116.

[70] S.-H. Lee, D.-K. Lee, C.-H. Shin, Y.-K. Park, P.A. Wright, W.M. Lee, S.B. Hong, J. Catal. 215 (2003) 151-170.

[71] S.I. Zones, C.Y. Chen, A. Corma, M.T. Cheng, C.L. Kibby, I.Y. Chan, A.W. Burton, J. Catal. 350 (2007) 41-54.

[72] D. Meloni, D. Martin, M. Guisnet, Appl. Catal. A 215 (2001) 67-79.

Marked up Revised manuscript

Click here to download Marked up Revised manuscript: Manuscript_annotated.docx

Click here to view linked References

Table 1. Physicochemical properties of commercial and home-synthesized zeolites.

Sample	$(Si/Al)_{bulk}$ ratio	$(Si/Al)_{surface}$ ratio[a]	Crystallite size (nm)	Crystal shape	S_{BET} (m^2/g)	S_{ext} (m^2/g)	V_{micro} (cm^3/g)
Z5SC	11.0	12.3	150	Spherical	391	39	0.17
Z5LC	10.4	9.7	1740x820x420	Parallelepiped	373	11	0.17
FER	8.9	10.0	370	Spherical	310	19	0.14
M22	10.5	12.1	860x80	Platelet	492	88	0.20
M22ox	13.9	20.0	870x80	Platelet	485	92	0.19
ITQ2	12.2	10.6	740x100	Platelet	649	324	0.13
IM5	12.9	13.8	710x250x250	Parallelepiped	345	12	0.16
TNU9	13.5	17.9	550x270x140	Parallelepiped	380	12	0.18

[a] From XPS measurements.

Table 2. Acidity results determined by the complementary techniques of NH_3-TPD, FTIR-pyridine, and FTIR- DTBPy.

Sample	NH_3-TPD		FTIR-pyridine		FTIR- DTBPy
	NH_3 uptake[a] (μmol /g)	T_{max} (ºC)	B250[b] (μmol /g)	B400[b] (μmol /g)	I_{3365}[c] (a.u.)
Z5SC	582	349	298	206	12
Z5LC	676	374	341	224	6
FER	767	404	170	157	13
M22	903	341	264	125	86
M22ox	669	385	238	114	57
ITQ2	409	321	230	85	185
IM5	816	378	371	178	6
TNU9	756	401	317	164	12

[a] NH_3 uptakes measured at 175ºC.

[b] Amounts of Brønsted acid sites measured at a pyridine desorption temperature of 250ºc (B250) and 400ºC (B400).

[c] Intensity (a.u.) of the stretching band at 3365 cm^{-1} for the protonated DTBPy after desorption of the probe base at 150ºC.

Figure captions

Figure 1. Powder X-ray diffraction patterns of calcined zeolites.

Figure 2. ^{27}Al MAS NMR spectra of hydrated H-zeolites. For a better comparison, the spectra have been normalized to the intensity of the tetrahedral (Al^{IV}) peak at ca. 52-54 ppm.

Figure 3. NH_3-TPD profiles of the H-zeolites.

Figure 4. H_2-TPR profiles for the CZA/zeolite hybrid catalysts (CZA:zeolite mass ratio of 2:1) normalized to the mass of CZA.

Figure 5. Correlation between the initial methanol dehydration rate of the zeolites and the density of strong Brønsted acid sites as determined by FTIR-pyridine at a desorption temperature of 400ºC. Methanol dehydration conditions: 260ºC, 1 bar, 10-20 mg of zeolite, MeOH:N_2 molar ratio = 20:80, total flow rate 75-150 cm^3/min (adjusted in each case to obtain initial methanol conversions of around 50%).

Figure 6. Relative methanol dehydration rates as a function of time-on-stream (TOS). Methanol dehydration conditions: 260ºC, 1 bar, 10-20 mg of zeolite, MeOH:N_2 molar ratio = 20:80, total flow rate 75-150 cm^3/min (adjusted in each case to obtain initial methanol conversions of around 50%).

Figure 7. Correlation between the relative loss of activity for methanol dehydration and the carbon content as determined by elemental analysis. Methanol dehydration conditions: 260ºC, 1 bar, 10-20 mg of zeolite, MeOH:N_2 molar ratio = 20:80, total flow rate 75-150 cm^3/min (adjusted in each case to obtain initial methanol conversions of around 50%).

Figure 8. Change of CO conversion with TOS in the syngas-to-DME reaction over CZA/Z hybrid catalysts (CZA:Z mass ratio of 2:1, hybrids prepared by grinding). Reaction conditions: 260ºC, 4.0 MPa, GHSV = 1700 $cm^3_{syngas}/(g_{cat}h)$, feed composition: 90 vol% (66 H_2/30% CO/4%CO_2) and 10 vol% Ar (internal standard for GC analyses). The dashed line represents the equilibrium CO conversion at the studied conditions.

Figure 9. Relative decrease of CO conversion during the syngas-to-DME experiments after ca. 50 h TOS ($-\Delta X_{CO}$) over CZA/zeolite hybrids as a function of: a) the zeolite external surface area (Sext) for two ranges of surface Al concentrations (given by the surface Al/(Si+Al) atomic ratios obtained by XPS), and b) the surface Al/(Si+Al) atomic ratio for two ranges of S_{ext}. Lines are only plotted as a guide to the eyes.

Figure 10. Correlation between the relative decrease of CO conversion ($-\Delta X_{CO}$) for CZA/zeolite hybrids and the parameter α, arbitrarily defined as $\alpha = [Al/(Si+Al)]_{XPS} \cdot S_{ext}$ (see text).

Figures

Fig. 1

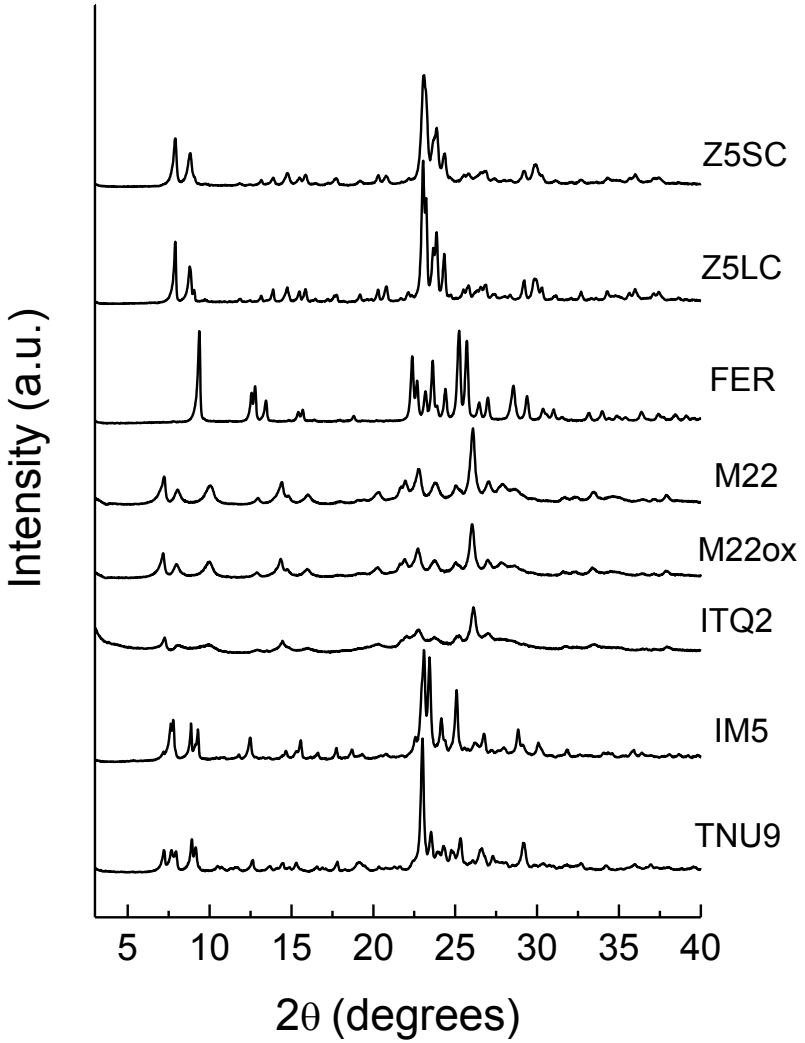

Fig. 2

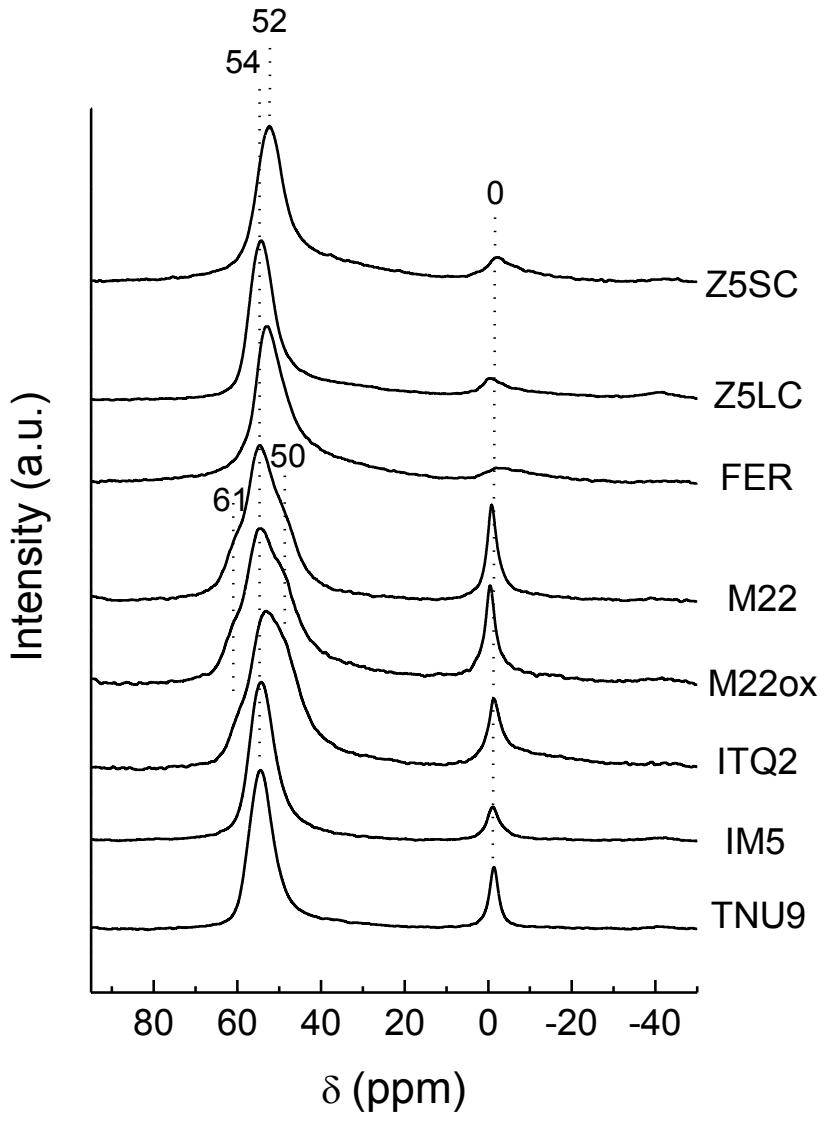
52
54
0
Z5SC
Z5LC
50
FER
61
M22
M22ox
ITQ2
IM5
TNU9
Intensity (a.u.)
80
60
40
20
0
-20
-40
δ (ppm)

Fig. 3

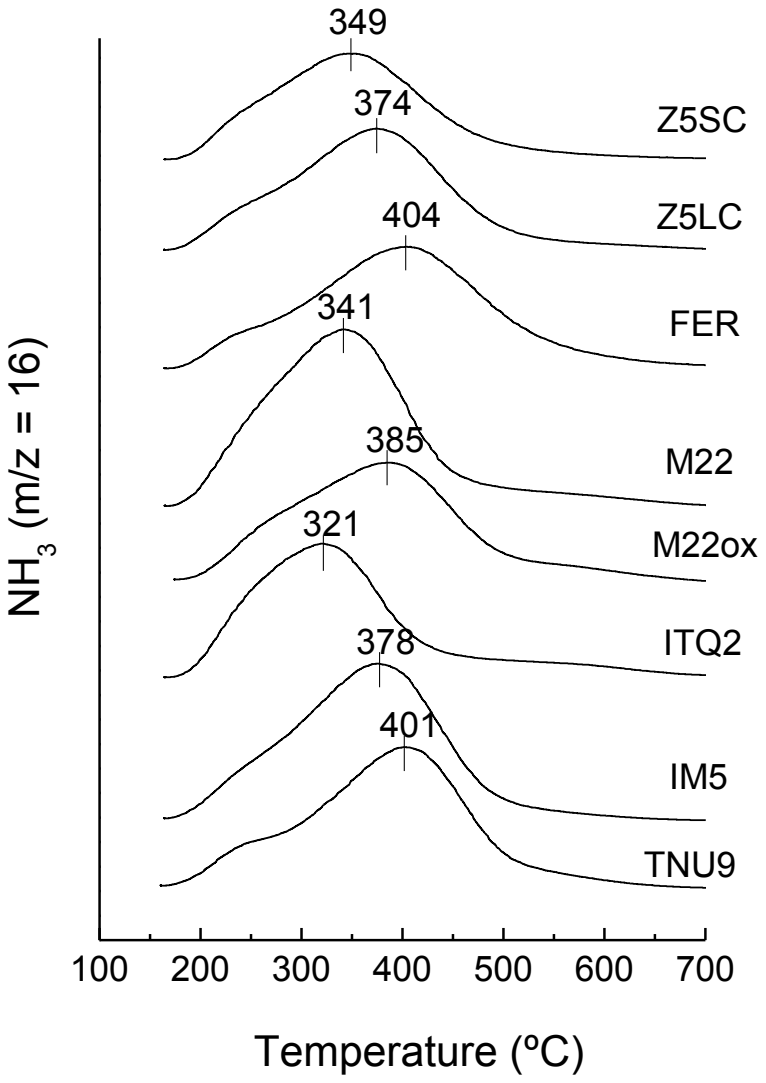
349
374
404
341
385
321
378
401
Z5SC
Z5LC
FER
M22
M22ox
ITQ2
IM5
TNU9
NH3 (m/z = 16)
100
200
300
400
500
600
700
Temperature (ºC)

Fig. 4

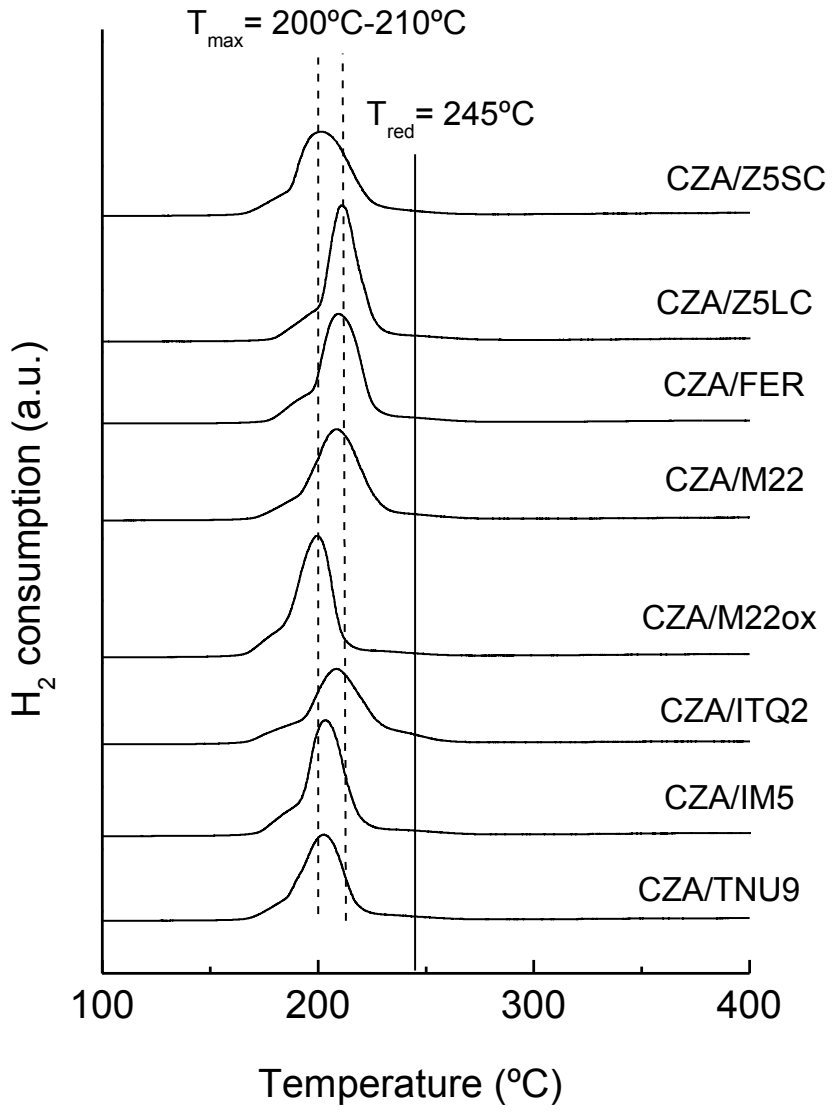
T max = 200ºC-210ºC
T red = 245ºC
CZA/Z5SC
CZA/Z5LC
CZA/FER
CZA/M22
CZA/M22ox
CZA/ITQ2
CZA/IM5
CZA/TNU9
H2 consumption (a.u.)
100
200
300
400
Temperature (ºC)

Fig. 5

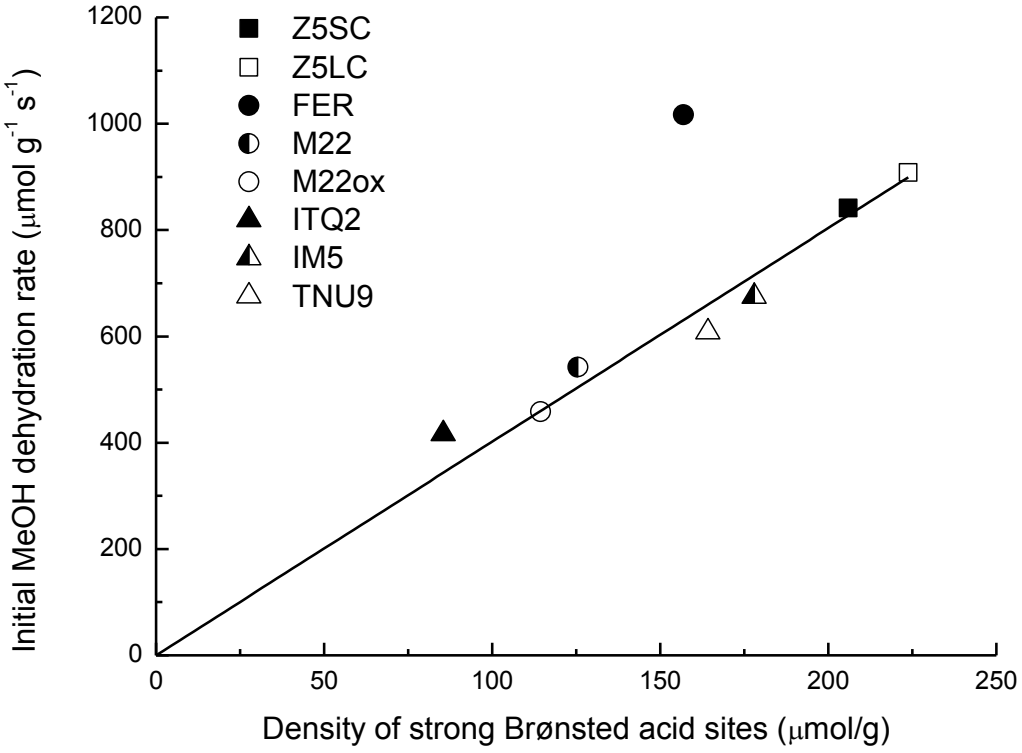
Initial MeOH dehydration rate (μmol g-1 s-1)
Density of strong Brønsted acid sites (μmol/g)
Z5SC
Z5LC
FER
M22
M22ox
ITQ2
IM5
TNU9
0
200
400
600
800
1000
1200
0
50
100
150
200
250

Fig. 6

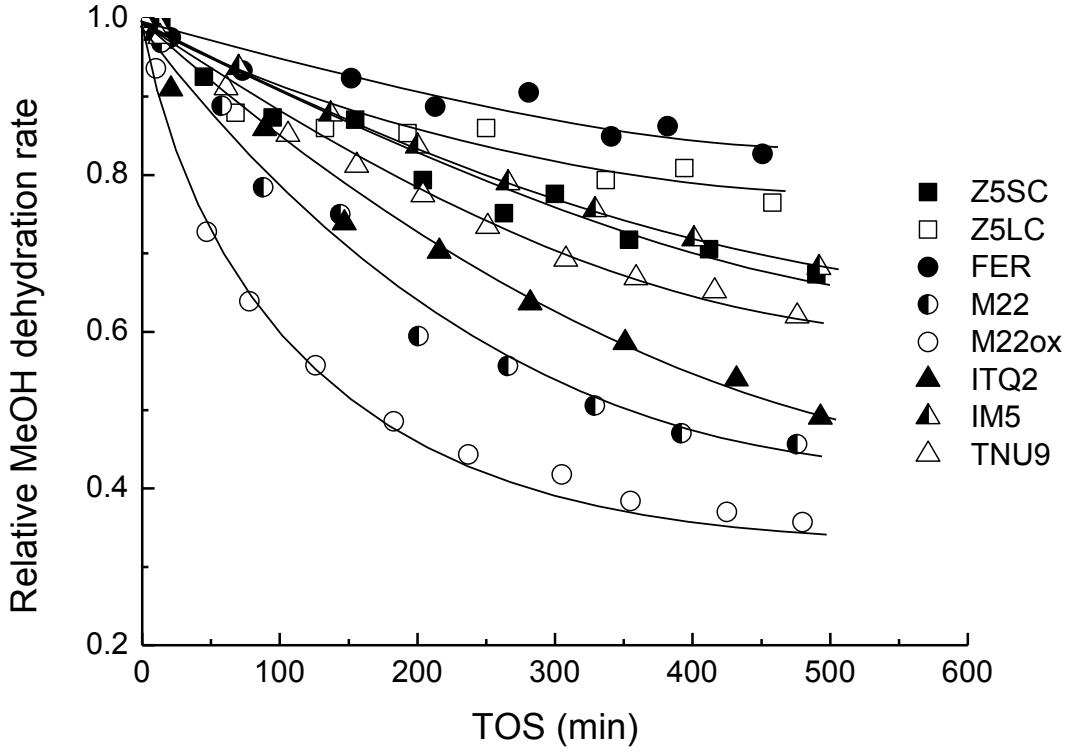
Relative MeOH dehydration rate
1.0
0.8
0.6
0.4
0.2
0
100
200
300
400
500
600
TOS (min)
Z5SC
Z5LC
FER
M22
M22ox
ITQ2
IM5
TNU9

Fig. 7

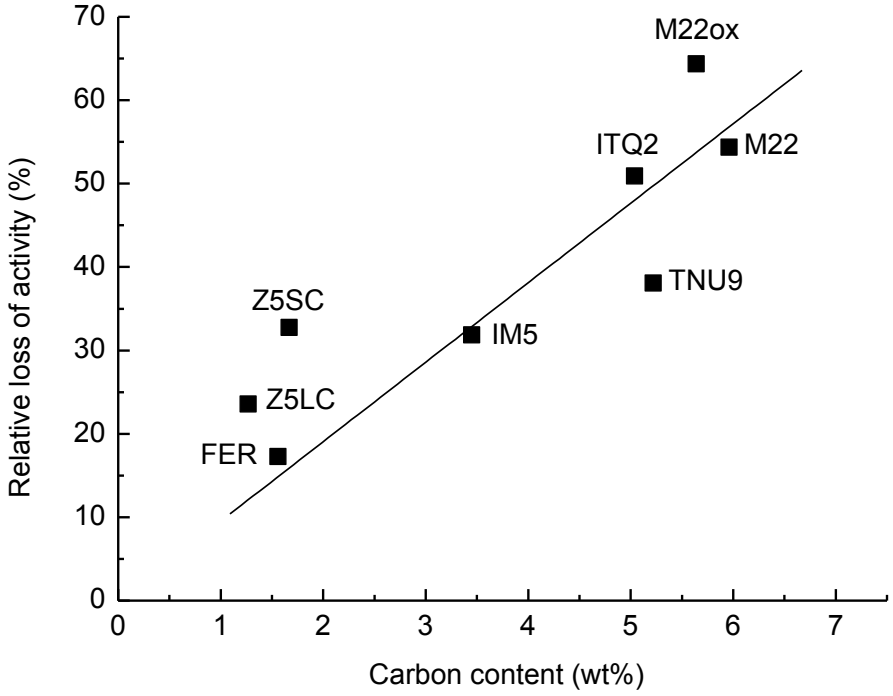
Relative loss of activity (%)
Carbon content (wt%)
0
10
20
30
40
50
60
70
0
1
2
3
4
5
6
7
M22ox
ITQ2
M22
TNU9
Z5SC
IM5
Z5LC
FER

Fig. 8

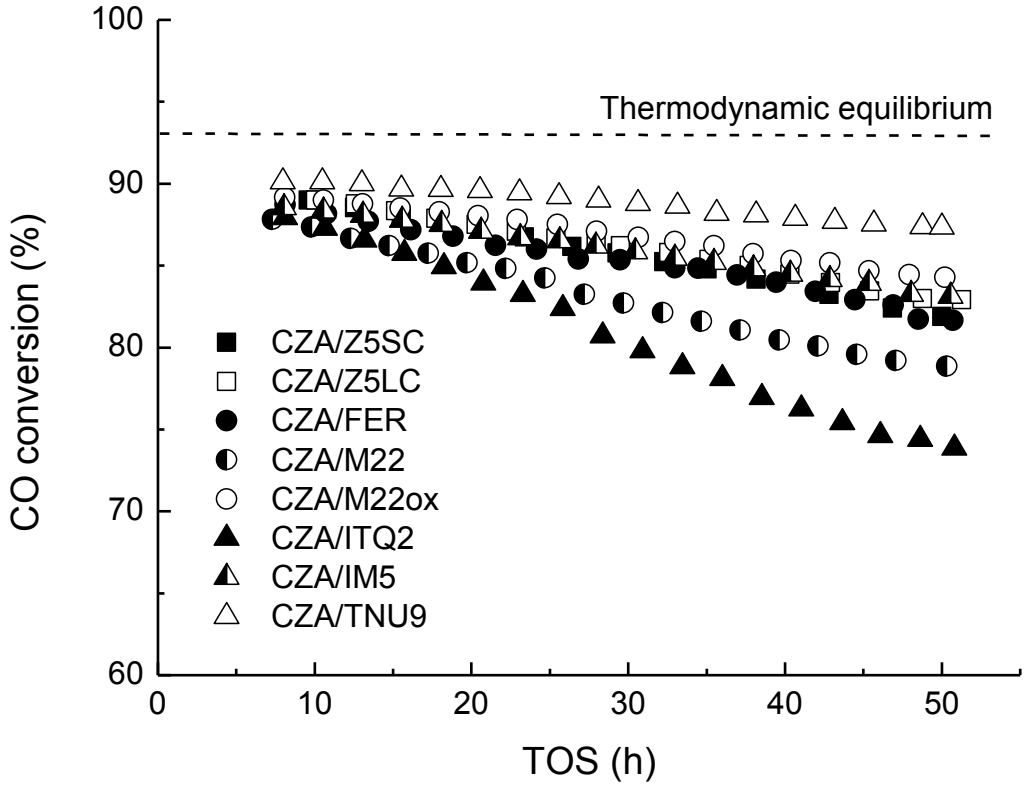
100
90
80
70
60
0
10
20
30
40
50
CO conversion (%)
TOS (h)
Thermodynamic equilibrium
CZA/Z5SC
CZA/Z5LC
CZA/FER
CZA/M22
CZA/M22ox
CZA/ITQ2
CZA/IM5
CZA/TNU9

Fig. 9

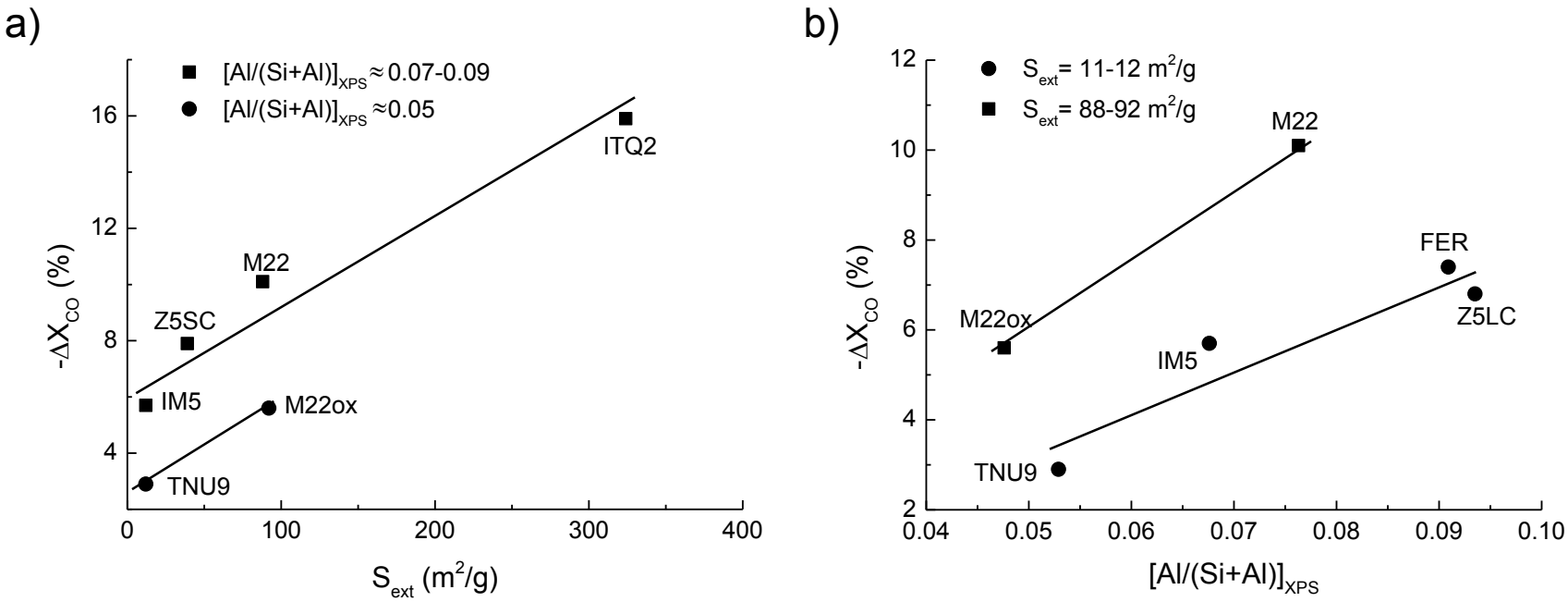
a)
[Al/(Si+Al)]XPS ≈ 0.07-0.09
[Al/(Si+Al)]XPS ≈ 0.05
ITQ2
M22
Z5SC
IM5
M22ox
TNU9
-ΔXCO (%)
Sext (m2/g)
b)
Sext = 11-12 m2/g
Sext = 88-92 m2/g
M22
FER
M22ox
Z5LC
IM5
TNU9
-ΔXCO (%)
[Al/(Si+Al)]XPS

Fig. 10

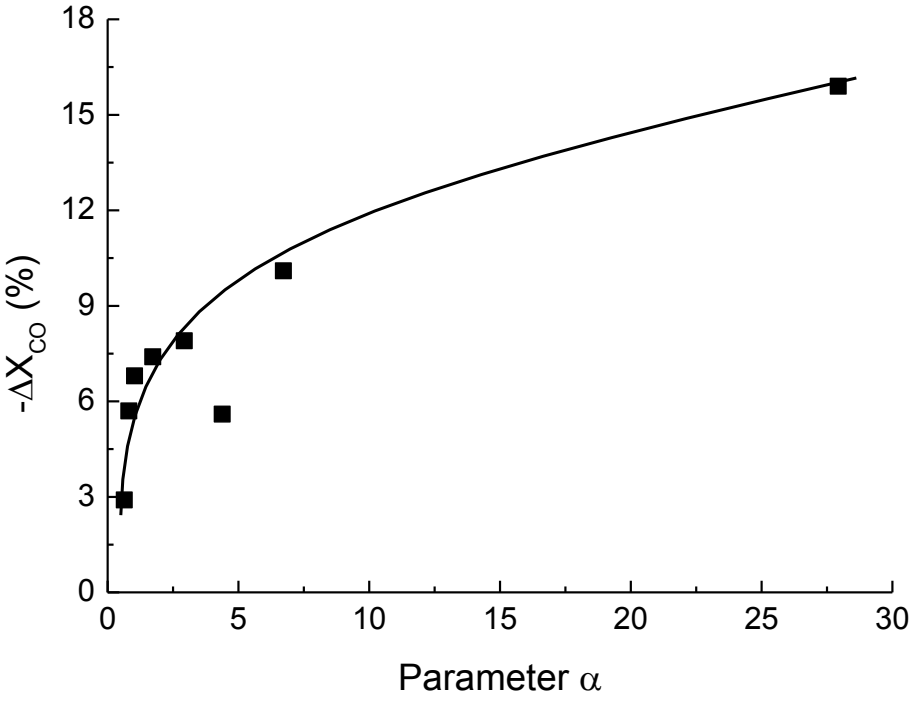

Supplementary Material

Click here to download Supplementary Material: Supplementary Material.docx

*Graphical Abstract (for review)

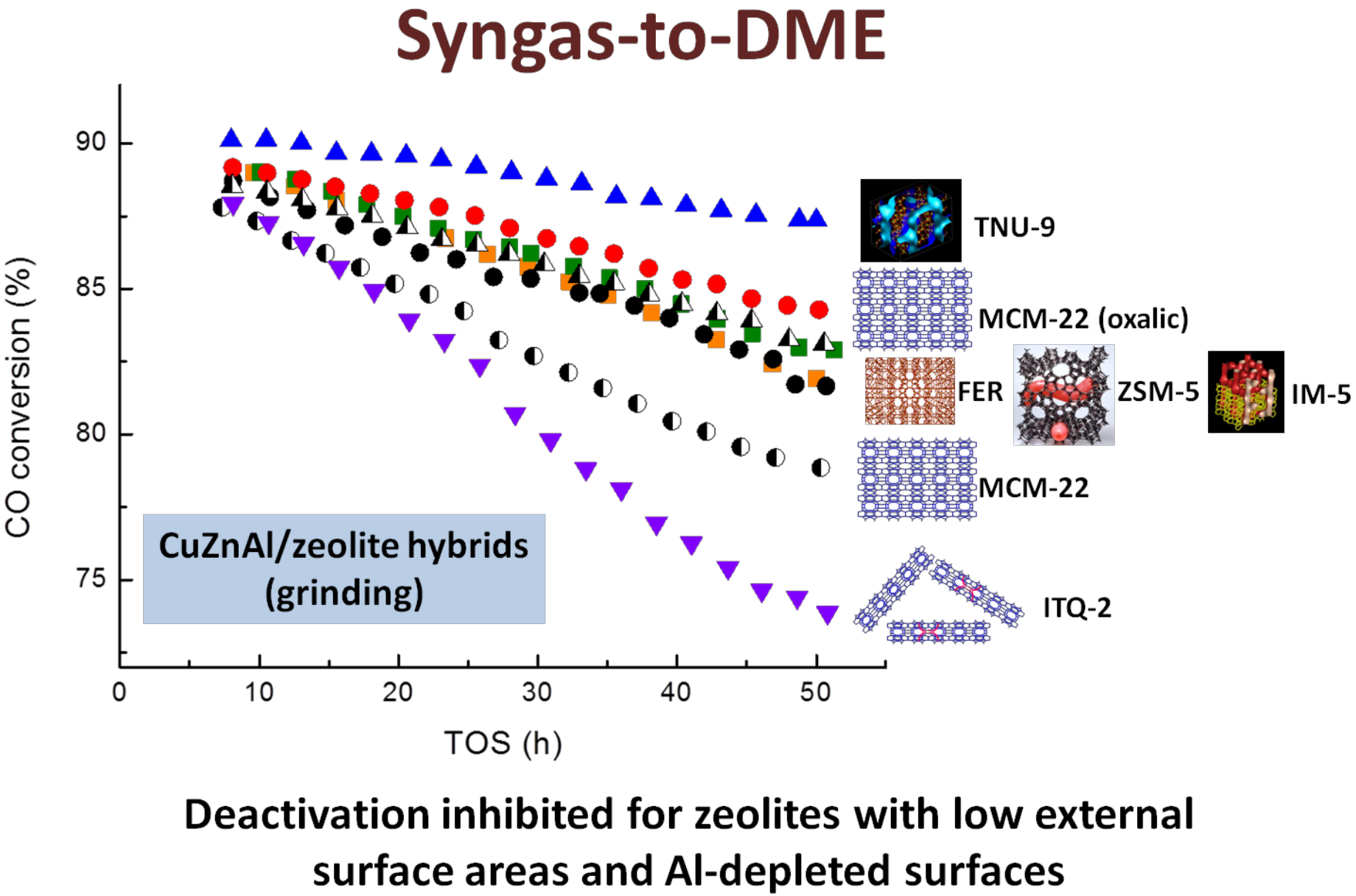

Highlights

- Six 10-ring pore zeolites (ZSM-5, FER, IM-5, TNU-9, MCM-22, ITQ-2) studied.
- Zeolite pore structure influences performance of hybrids in syngas-to-DME.
- Extent of deactivation increases with amount of surface aluminum and external area.
- Deactivation of hybrids related to CuZnAl-zeolite interactions.